GPS Solutions (2023) 27:37
https://doi.org/10.1007/s10291-022-01361-w

ORIGINAL ARTICLE

Improving GNSS carrier phase tracking using a long coherent integration architecture

Xin Feng[1] · Tisheng Zhang[1,2] · Xiaoji Niu[2] · Thomas Pany[3] · Jingnan Liu[1,2]

Received: 28 May 2022 / Accepted: 30 October 2022 / Published online: 13 December 2022
© The Author(s), under exclusive licence to Springer-Verlag GmbH Germany, part of Springer Nature 2022

Abstract

High-sensitivity carrier phase tracking is essential for new GNSS high-precision applications such as unmanned vehicles and smartphones. Increasing coherent integration time is the primary way to improve the sensitivity of carrier phase tracking, which is, however, significantly restricted by the receiver local oscillator instability. We propose a long coherent integration (LCI) architecture to improve carrier phase tracking. The architecture is equipped with a multichannel cooperative loop to track receiver oscillator errors and local loops to perform super-long coherent integration periods. The transfer function of LCI tracking loops is established in s-domain, and the tracking error models induced by thermal noise and Allan deviation oscillator phase noise are derived in z-domain. The performance of the LCI tracking architecture is tested through both simulation and actual GNSS signals. The proposed error models of LCI are validated through the semi-analytic simulation. Both simulation and real signal testing results indicate that LCI tracking loops can perform coherent integration up to 3 s and track extremely weak signals of 6 dB-Hz with carrier phase accuracy of around 4 degrees.

Keywords Long coherent integration · Carrier phase · Oscillator instability · Phase locked loop · Tracking loop

Introduction

GNSS (Global Navigation Satellite System) plays a significant role in the family of localization techniques for its capability of providing 24/7 cm accurate positioning when real-time kinematic (RTK) algorithm is used. Accurate and robust localization ability is the prerequisite for an autonomous vehicle to operate safely and effectively (Kuutti et al. 2018). In addition, the submeter-level high-precision positioning applied to the low-cost GNSS chipsets in intelligent mobile terminals, such as smartphones, is the general trend (Zhang et al. 2018). However, the availability of GNSS remains a challenge (Bresson et al. 2017). The performance of GNSS degrades severely in urban environments where the mixture of multipath interference, non-line-of-sight signal reception and signal intensity degradation will reduce the localization accuracy to several meters or even make GNSS unavailable. Increasing coherent integration time is a radical method to improve GNSS receiver sensitivity and mitigate multipath (O Driscoll et al. 2011). It is a common assumption that a receiver integration time should be less than dozens of milliseconds (Pany et al. 2009). Therefore, it is reasonable to consider the integration period longer than 100 ms as long coherent integration time. Focal point developed supercorrelation to improve the sensitivity and accuracy for pseudorange and Doppler measurements (Groves et al. 2020). In terms of GNSS carrier phase tracking, the sensitivity of a typical GNSS receiver is only around 25 dB-Hz, which is far from the positioning requirement of applications of autonomous vehicles or intelligent terminals.

To increase coherent integration time effectively, there are three major obstacles to overcome, which are navigation bit transition, user dynamics and oscillator clock instability (Alban et al. 2003). The former two factors are relatively easier, and mature solutions are developed. In the presence of reference base stations, one can use assisted GNSS (AGNSS) to eliminate the impact of navigation bit transition (Van Diggelen 2009). For a stand-alone GNSS receiver, a navigation bit prediction algorithm can be applied (Ren and

✉ Tisheng Zhang
zts@whu.edu.cn

1 School of Geodesy and Geomatics, Wuhan University, Wuhan 430079, China

2 Integrated & Intelligent Navigation (I2Nav) Group, GNSS Research Center, Wuhan University, Wuhan 430072, China

3 Universität Der Bundeswehr München, Neubiberg, Germany

Petovello 2017). Besides, some new GNSS signals, such as Galileo E5a/b, and Beidou B2a/b, are modulated with pilot signals and navigation bit transition is no longer a problem when tracking these signals (Rebeyrol et al. 2007; Zhang et al. 2019). To eliminate the impact of the relative receiver-satellite motion, an inertial measurement unit (IMU) is often employed. Known as ultra-tight or deep integration of GNSS and inertial navigation system (INS), related research over the past decades has proven that with the assistance of an IMU, GNSS carrier phase lock loops (PLLs) can work under quasi-static conditions (Pany et al. 2005, 2009; Bernal et al. 2008; Zhang et al. 2017). Niu et al. (2015) assess the performance of INS-aided PLLs of different grades of IMUs theoretically. The results show that the maneuver-independent velocity errors of MEMS IMUs cause the carrier phase tracking errors below 1.2 degrees. Zhang et al. (2017) prove that the carrier phase error from the MEMS INS-aided PLLs almost remains the same as when they are under static conditions through real high dynamic field tests. Ultra-tight GNSS/INS integration has been validated as an efficient approach to eliminating the dynamics in long coherent integration (Pany et al. 2009; Soloviev and Dickman 2011; Ren and Petovello 2017). But the oscillator instability still remains challenging. Therefore, navigation bit transition and user dynamics will be presumed solved by the methods mentioned above. Our main focus is to reduce the adverse effect of oscillator instability during the process of long time coherent integration.

The oscillator phase noise is divided into long-term trends and short-term stochastic processes of phase and frequency (Curran et al. 2012). Both factors will reduce the performance of tracking loops. The effect of oscillator instability on coherent integration time has been widely studied (Gaggero 2008; Gowdayyanadoddi et al. 2014; Watson et al. 2006; Thombre et al. 2011). Ultra-stable oscillators can support up to dozens of seconds of integration time, which is essential for high-sensitivity GNSS applications. However, consumer grade GNSS receivers still cannot afford the cost of high performance ultra-stable oscillators. In consequence, the PLLs must be carefully designed to cope with the instability of local oscillators (Irsigler and Eissfeller 2002).

The techniques to deal with oscillator instability in GNSS receivers can be separated into two main categories: difference-based methods and estimation-based methods. The difference correlator, a novel tracking approach proposed by Pany et al. (2011), performs correlator level single and double difference between rover and base station, so common clock errors can be eliminated and extremely long integration time are possible. Estimation-based methods try to estimate the modulated clock drift in some way. With appropriate modeling of oscillator phase noise, Wiener or Kalman filter can be applied to the design of GNSS PLL (Curran et al. 2012; Chen et al. 2017). Zhodzishsky et al. (1998) proposed Co-Op tracking loops, which utilize four filters to track receiver position errors and oscillator bias. Based on Co-Op tracking loops, we (Zhuo 2019) developed a carrier phase tracking architecture that utilizes multiple correlator information to estimate oscillator phase noise. Zhodzishsky et al. (2020) proposed a quartz locked loop (QLL) system, which applies a common loop to track errors caused by oscillator vibrations to increase the vibration resistance of GNSS receivers. The difference-based methods rely on high-quality base station observations, which are not always available in practical applications. The estimation-based methods usually utilize the mathematical models of oscillators, which are not precise enough in practice and few of them implement long coherent integration.

In light of combining multiple correlators to estimate oscillator phase errors, we propose the long coherent integration (LCI) architecture that is capable of estimating the oscillator phase errors independently and accurately, facilitating long coherent integration. In the subsequent section, the methodology of the LCI architecture is introduced. Afterward, a complete theoretical frequency domain model of the LCI tracking loops is developed based on the LCI methodology. Finally, the performance of LCI loops will be investigated through both semi-analytic simulations and static field tests.

LCI tracking methodology

This section introduces the methodology of the proposed long coherent integration (LCI) architecture. An overall diagram of LCI architecture will be given in the first place. Then two key techniques will be described in detail. One is the multi-cooperative loop discriminator, which is designed to estimate the effects of oscillator instability, and the other is the implementation of local long coherent integration.

Overall scheme of LCI tracking architecture

As shown in Fig. 1, based on the typical structure of GNSS receivers, the LCI tracking architecture adds a multichannel cooperative loop to track the common source of errors such as oscillator instability. Each channel's local loop closure tracks the residual carrier phase and its specific errors, such as atmospheric delays.

Details of local tracking loops are displayed with blue background on top of Fig. 1. Each channel's numerical controlled oscillator (NCO) is controlled by two quantities, one of which is from the filter of the local channel itself ($u_i, i = 1, 2, 3 \ldots$), and the other one is from the multichannel cooperative loop (v). Taking correlator values of all channels as input, the first module of the multichannel cooperative loop is a channel sieve that screens out the channels with

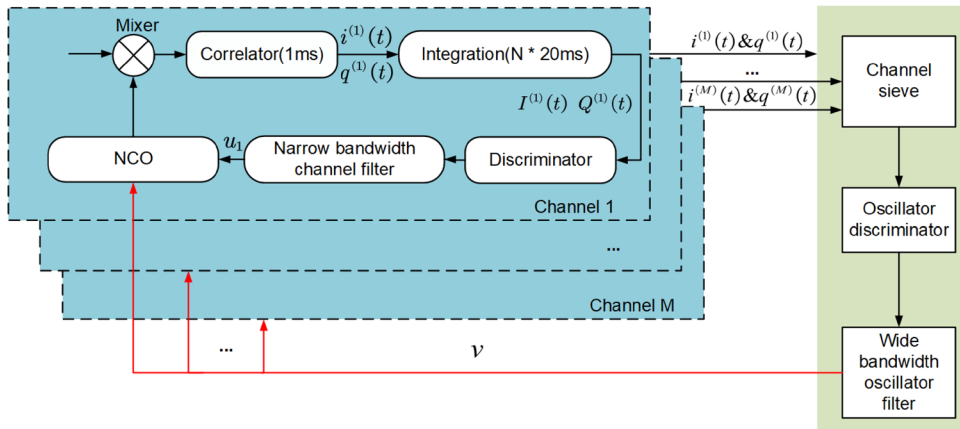

Fig. 1 Overall diagram of LCI tracking architecture. The blue presents the M local tracking channels and their internal structure, and the yellow presents the multichannel cooperative loop. The multichannel cooperative loop takes correlator values of all channels as input and outputs the oscillator phase noise estimation which is used to assist local loop tracking

a weak signal. This step is to ensure each channel used to estimate the oscillator error carries a low thermal noise level so that the oscillator discriminator can accurately extract the effects of clock instability. Two factors are considered in the process of selecting strong signal strength channels. One is the carrier-to-noise ratio (C/N_0), and the other is the elevation angle. Satellites with higher elevation angles often indicate they have stronger signal strength and are less sensitive to the dynamics with slowly varying altitude, for example the vehicle dynamics. If the C/N_0 value and elevation angle both exceed the determined thresholds, the satellite will be used to estimate the oscillator error. If there are no satellites with elevation angles high enough, channel sieve will select the channels with an elevation-independent C/N_0 threshold.

The coherent integration time of the local channel is set as multiples of the length of a navigation bit, for example 20 ms for GPS L1 C/A. During the initialization process, the local loop performs 20 ms coherent time, and the bandwidth of the channel filter is set as narrow as possible to reduce the thermal noise so that the effects of oscillator instability will "manifest." After control information from the multichannel cooperative loop takes effect, a much longer integration time for the local channel can be performed.

Multichannel cooperative loop discriminator

The radio frequency (RF) GNSS signal incident on the receiver antenna will be down-converted to an intermediate frequency (IF), which will be correlated with local in-phase and quadrature replicas to estimate the carrier parameters. The correlation period is usually the length of a spreading code, for example 1 ms for GPS L1 C/A. After correlation, the signal is expressed as:

$$i(n) = D(n)R(\tau)\cos(\delta\theta(n)) \tag{1}$$

$$q(n) = D(n)R(\tau)\sin(\delta\theta(n)) \tag{2}$$

where $D(n)$ represents the spreading code and navigation bit sequence, τ and $\delta\theta(n)$ denote the code and carrier phase error, and $R(\cdot)$ is the auto-correlation function of code error.

Correlator values will be directed into two paths. One path is the local channel integration module, and the other is the channel sieve of the common loop. Both paths will integrate the correlator results, but with different coherent integration time. The integrated signal has the following expression:

$$I(n) = D(n)\sin c\left(f_e T_{coh}\right)\cos\left(\theta_e\right) \tag{3}$$

$$Q(n) = D(n)\sin c\left(f_e T_{coh}\right)\sin\left(\theta_e\right) \tag{4}$$

where T_{coh} denotes the integration time, f_e and θ_e represent the average frequency and phase error during the integration period. Since our main concerns are the effects of receiver clock instability and thermal noise, the effect of dynamics is presumed eliminated from the tracking loops already. The phase errors are expressed as:

$$\theta_e = \theta_r + \theta_c \tag{5}$$

where θ_r and θ_c denote the thermal noise and oscillator clock phase noise. All the channels selected by the channel sieve will be utilized by a well-designed oscillator discriminator to estimate the oscillator phase error.

Multichannel cooperative discriminator takes a group of signals $I^1, Q^1 ... I^N, Q^N$ as input to estimate the clock phase error. As mentioned above, the phase error of the signal after integration consists of two components: oscillator clock phase noise θ_c, which is the same in each channel, and thermal noise θ_r, which is mutually independent of each other. Intuitively, averaging the phase errors of all channels results in an accurate clock phase error estimation, which is the aim of multichannel cooperative discriminator designing:

$$\widetilde{\theta}_c = \frac{\sum_{i=1}^{N} \theta_e^{(i)}}{N} = \frac{\sum_{i=1}^{N} (\theta_r^{(i)} + \theta_c^{(i)})}{N} \tag{6}$$

where N is the number of channels used to estimate the clock phase error.

Considering the phase error of one loop first, the phase error of channel i can be estimated by:

$$\tilde{\theta}_e^{(i)} \approx I^{(i)} Q^{(i)} = \left(D^{(i)} \sin c(f_e^{(i)} T_{coh})\right)^2 \sin\left(2\theta_e^{(i)}\right) \tag{7}$$

The equation above is a classic Costas loop discriminator whose output error is $\sin\left(2\theta_e^{(i)}\right)$ and the slope of the output error is proportional to signal amplitude squared (Kaplan and Hegarty 2017).

In order to estimate the clock phase error cooperatively, the output errors of multiple channels should be normalized by the signal amplitudes squared, which can be estimated using $\left(I^{(i)}\right)^2$ for the signal power concentrates in the I branch, resulting in the multichannel cooperative discriminator:

$$\widetilde{\theta}_c = \frac{\sum_{i=1}^{N} I^{(i)} Q^{(i)}}{\sum_{i=1}^{N} I^{(i)2}} \tag{8}$$

Inserting (3) and (4) in the equation above results in:

$$\widetilde{\theta}_c = \frac{\sum_{i=1}^{N} (D^{(i)} \sin c(f_e^{(i)} T_{coh}))^2 \sin\left(2\theta_e^{(i)}\right)}{\sum_{i=1}^{N} (D^{(i)} \sin c(f_e^{(i)} T_{coh}))^2 \left(\cos\left(\theta_e^{(i)}\right) + 1\right)} \tag{9}$$

When the local loop enters the stable tracking state, the frequency error can be assumed to be 0. In other words, $(D^{(i)} \sin c(f_e^{(i)} T_{coh}))^2 \approx 1$. Also, when the phase error approaches 0, the first terms of the Taylor series of $\cos(\cdot)$ and $\sin(\cdot)$ are used as their approximate values. By doing so,

$$\begin{aligned} \widetilde{\theta}_c &\approx \frac{\sum_{i=1}^{N} 2\theta_e^{(i)}}{\sum_{i=1}^{N} (1+1)} = \frac{\sum_{i=1}^{N} \theta_e^{(i)}}{N} \\ &= \frac{\sum_{i=1}^{N} (\theta_r^{(i)} + \theta_c^{(i)})}{N} \end{aligned} \tag{10}$$

Since the oscillator instability has the same effect on all satellite channels, $\theta_c^{(1)} = \cdots = \theta_c^{(N)}$, and the thermal noise of each channel is assumed to be white and independent to each other, (8) indicates that the oscillator discriminator calculates the average value of measurements of clock-induced error from every channel.

Long coherent integration of local loop

With a multichannel cooperative loop tracking the effects of oscillator instability and the assistance of external navigation bits, the long coherent integration process can be expressed as:

$$\begin{aligned} I_L^{(i)} &= \sum_{k=1}^{N_L} P(k) I_B^{(i)}(k) \\ Q_L^{(i)} &= \sum_{k=1}^{N_L} P(k) Q_B^{(i)}(k) \end{aligned} \tag{11}$$

where $P(k)$ is the polarity of kth navigation bit. The long coherent integration is realized through the accumulation of N_L successive one navigation bit long integrations. $I_B^{(i)}(k)$ and $Q_B^{(i)}(k)$ denote the fundamental coherent integration signal with the length of a navigation bit, which will be, for example, 20 ms for GPS L1 signal. They are expressed as:

$$\begin{aligned} I_B^{(i)}(k) &= \sum_{j=1}^{N_B} i^{(i)}\left(kN_B + j\right) \\ Q_B^{(i)}(k) &= \sum_{j=1}^{N_B} q^{(i)}\left(kN_B + j\right) \end{aligned} \tag{12}$$

If the correlation period is 1 ms, N_B will be 20 for GPS L1 signal. The normalized complex long coherent integration signal is expressed as:

$$\mathbf{r}(n) = \sin c\left(f_e T_{coh}\right) e^{j\theta_e} \tag{13}$$

Amplitude of the signal is shown in Fig. 2, where the integration periods of 20 and 40 ms are adopted. The constant Doppler offset leads to a power attenuation following the sinc-squared characteristic. With the same Doppler offset, e.g., 10 Hz in Fig. 2, the longer the integration time is, the greater the power attenuation is going to be.

As shown in Fig. 3, multichannel cooperative and local loops have different coherent summation interval length. High-frequency update of the multichannel cooperative

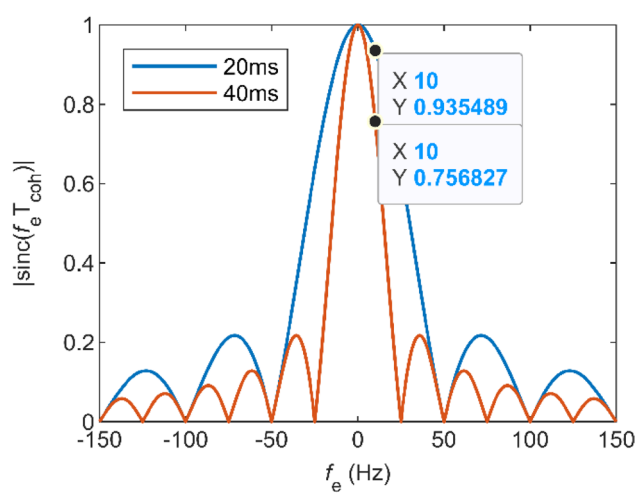

Fig. 2 Amplitude of integration signal. The blue and red lines present 20 and 40 ms of integration periods, respectively

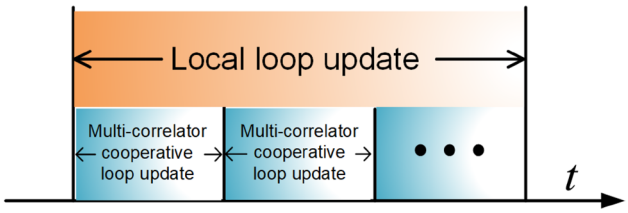

Fig. 3 Update diagram of local and multichannel cooperative loops. The orange presents a long coherent local loop update period during which the multichannel cooperative loop updates multiple times

loop makes sure that the frequency error induced by receiver oscillator instability fluctuates around 0 and does not drift away. Furthermore, it is worth noting that time epochs for discriminator or correlator values in (6) or (8) are slightly different for each channel, as the integrate and dump periods within the receiver are synchronized the PRN code periods and the PRN codes arrive a different times at the receiver. During the summation over N channels in (6) or (8), only those epochs that are nearest to each other are considered. As shown in the left part of Fig. 4, local oscillator dynamics is low enough such that this minor synchronization mismatch has no impact on the later LCI.

The discriminator outputs of a typical PLL and an LCI local loop based on real static open sky GPS L1 signals are shown in Fig. 4 to justify the validity of LCI tracking architecture. For PLL tracking loops with 100 ms coherent integration time and 1 Hz bandwidth, the discriminator outputs of three GPS satellite channels are shown in the left subfigure of Fig. 4. It is evident that these lines follow the same pattern, which is apparently caused by the effects of a common error resource: the receiver oscillator instability. Test results in the right subfigure of Fig. 4 are conducted using the LCI tracking method with a 10 ms, 15 Hz multichannel cooperative loop and 100 ms, 1 Hz local loops. The effects due to oscillator instability are tracked and compensated by the multichannel cooperative loop, so the local loops should only care about the thermal noise.

Modeling of LCI tracking loop

Since the LCI tracking architecture is newly proposed, the traditional measurement error model of PLL loops cannot be applied to the LCI loops. An LCI measurement error model is needed to provide theoretical guidance for practical use. Based on the time domain LCI tracking methodology of the previous section, the LCI theoretical model in the frequency domain will be developed in this section.

LCI loop transfer function derivation

The s-domain model of LCI tracking loops is shown in Fig. 5. Loop discriminator is modeled as the difference of carrier phase between the received signal and local replica, and the oscillator discriminator is modeled as the average of carrier phase errors from multiple channels selected by the channel sieve. From Fig. 5, the ith channel model can be expressed as:

$$\theta_e^{(i)} = \phi^{(i)} - \gamma^{(i)} \tag{14}$$

$$\gamma^{(i)} = \frac{F(s)}{s}\theta_e^{(i)} + \frac{G(s)}{s}\frac{1}{N}\sum_{k=1}^{N}\theta_e^{(k)} + \gamma_{clk} \tag{15}$$

where $\phi^{(i)}$ and $\gamma^{(i)}$ denote the input and output signal phase of the local loop, respectively; $F(s)$ and $G(s)$ denote the transfer function of the filter of the local and multichannel cooperative loop, respectively. The receiver maintains the tracking of M channels and only $N(M \geq N)$ channels are selected to estimate the effect of oscillator instability. Inserting (14) in (15) results in:

$$\begin{aligned}\left(1 + \frac{F(s)}{s}\right)\gamma^{(i)} + \frac{G(s)}{s}\frac{1}{N}\sum_{k=1}^{N}\gamma^{(k)} \\ = \frac{F(s)}{s}\phi^{(i)} + \frac{G(s)}{s}\frac{1}{N}\sum_{k=1}^{N}\phi^{(k)} + \gamma_{clk}\end{aligned} \tag{16}$$

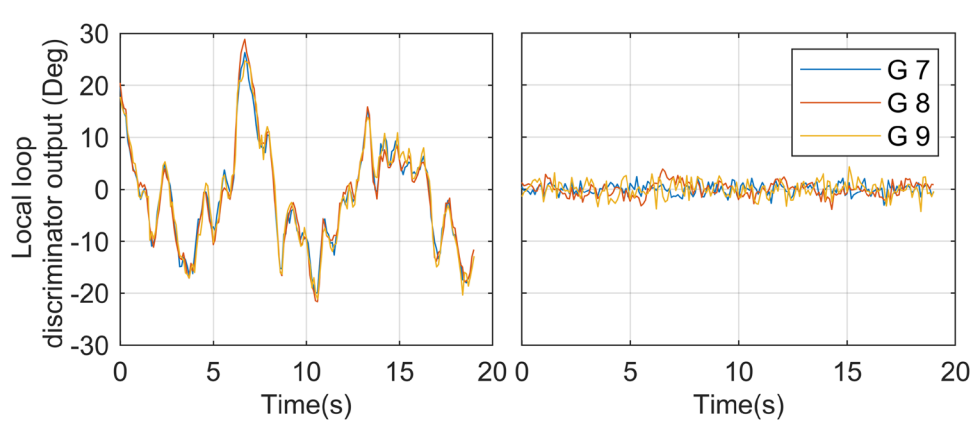

Fig. 4 Discriminator outputs of local loops. The left and right panel shows the local loop discriminator output of a PLL and the LCI architecture, respectively

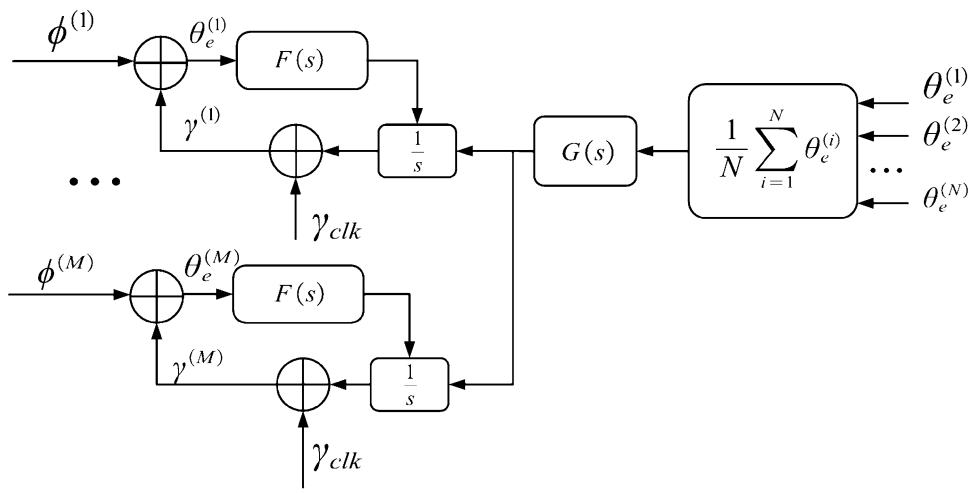

Fig. 5 Laplace model of LCI tracking loops. The multichannel cooperative loop discriminator is modeled as the average of phase errors from channels selected by the channel sieve

Since a channel model is dependent on other channels, considering all satellite channels as a whole is necessary.

For M tracking channels, define the following expressions:

$$\begin{aligned}
&\beta_1 = 1 + \frac{F(s)}{s}, \beta_2 = \frac{G(s)}{s}, \beta_3 = \frac{F(s)}{s} \\
&\mathbf{e} = \left[11 \ldots 1\right]^T, \mathbf{d} = \left[\mathbf{d_s} 0\right]^T \\
&\boldsymbol{\gamma} = [\gamma^{(1)}\gamma^{(2)} \ldots \gamma^{(M)}]^T \\
&\boldsymbol{\phi} = [\phi^{(1)}\phi^{(2)} \ldots \phi^{(M)}]^T
\end{aligned} \tag{17}$$

where $\mathbf{d}$ is constructed by adding $0^{\boldsymbol{T}} = [0, 0, \ldots, 0]^T$ of length $M - N$ at the end of the vector $\mathbf{d_s} = [\frac{1}{N}\frac{1}{N} \ldots \frac{1}{N}]^T$ of length N. Expanding (16) to M channels leads to the overall s-domain model of LCI tracking loops:

$$(\beta_1 \mathbf{I} + \beta_2 \mathbf{e}\mathbf{d}^T)\boldsymbol{\gamma} = (\beta_3 \mathbf{I} + \beta_2 \mathbf{e}\mathbf{d}^T)\boldsymbol{\phi} + \mathbf{e}\gamma_{clk} \tag{18}$$

The output carrier phase contains two independent components, namely white Gaussian noise $\boldsymbol{\gamma}_r$ and clock phase noise $\boldsymbol{\gamma}_c$:

$$\boldsymbol{\gamma} = \boldsymbol{\gamma}_r + \boldsymbol{\gamma}_c \tag{19}$$

Therefore, Eq. (18) can be separated to two equations which will be solved respectively.

$$(\beta_1 \mathbf{I} + \beta_2 \mathbf{e}\mathbf{d}^T)\boldsymbol{\gamma}_r = (\beta_3 \mathbf{I} + \beta_2 \mathbf{e}\mathbf{d}^T)\boldsymbol{\phi} \tag{20}$$

$$(\beta_1 \mathbf{I} + \beta_2 \mathbf{e}\mathbf{d}^T)\boldsymbol{\gamma}_c = \mathbf{e}\gamma_{clk} \tag{21}$$

Equations (20) and (21) can be solved by multiplying the Sherman–Morrison inversion of $(\beta_1 \mathbf{I} + \beta_2 \mathbf{e}\mathbf{d}^T)$ on both sides of them:

$$(\beta_1 \mathbf{I} + \beta_2 \mathbf{e}\mathbf{d}^T)^{-1} = \beta_1^{-1} - \frac{\beta_2 \beta_1^{-1} \boldsymbol{e}\mathbf{d}^T}{\beta_1 + \beta_2}$$

$$\boldsymbol{\gamma}_r = \left(\beta_1^{-1} - \frac{\beta_2 \beta_1^{-1} \boldsymbol{e}\mathbf{d}^T}{\beta_1 + \beta_2}\right)(\beta_3 \mathbf{I} + \beta_2 \mathbf{e}\mathbf{d}^T)\boldsymbol{\phi}$$

$$\boldsymbol{\gamma}_c = (\beta_1^{-1} - \frac{\beta_2 \beta_1^{-1} \boldsymbol{e}\mathbf{d}^T}{\beta_1 + \beta_2})\mathbf{e}\gamma_{clk} \tag{22}$$

Equation (22) is the foundation of the following derivation, where tracking errors induced by oscillator phase noise and thermal noise will be analyzed separately.

Tracking error induced by oscillator phase noise

The transfer function of a specific channel associated with oscillator phase noise γ_c can be derived from (22):

$$H_{clk}(s) = \frac{\gamma_{clk}^{(i)}}{\gamma_c^{(i)}} = \frac{1}{\beta_1 + \beta_2} = \frac{s}{s + F(s) + G(s)} \tag{23}$$

In order to estimate the tracking error induced by oscillator instability, the mathematical model of an oscillator should be established. The oscillator phase noise power spectral density (PSD) is modeled (Irsigler and Eissfeller 2002) as:

$$S_c(\omega) = (2\pi f_0)^2 \frac{S_y(\omega)}{\omega^2} \tag{24}$$

where f_0 is the carrier frequency and $S_y(\omega)$ denotes the oscillator fractional frequency deviation:

$$S_y(\omega) = \frac{2\pi^2 h_{-2}}{\omega^2} + \frac{\pi h_{-1}}{\omega} + \frac{h_0}{2} + \frac{h_1 \omega}{4\pi} + \frac{h_2 \omega^2}{8\pi^2} \tag{25}$$

where h_i are oscillator quality related constant coefficients. The specific description of each coefficient can be found in the research of Curran et al. (2012). Among all the h-parameters, h_1 and h_2 have an insignificant impact on the tracking loop performance and it is impossible to factorize h_{-1} into

rational PSD. As a result, only h_0 and h_{-2} are considered in the analysis.

Oscillator phase noise-induced tracking error can be derived through (23) and (25),

$$\sigma_{clk}^2 = \frac{1}{2\pi}\int_0^{\infty} |H_{clk}(\omega)|^2 S_c(\omega) d\omega \tag{26}$$

According to Shafaati et al. (2015), spectral factorization and contour integrals are employed to simplify the evaluation of the equation above, which results in:

$$\sigma_{clk}^2 = \frac{1}{2\pi j}\int_{-j\infty}^{+j\infty} H_{clk}(s) S_c^+(s) ds \tag{27}$$

where all $S_c^+(s)$ poles reside on the left side of the complex plane, which is denoted as:

$$S_c^+(s) = (2\pi f_0)\left(\frac{\sqrt{0.5h_0}s + \sqrt{2\pi^2 h_{-2}}}{s^2}\right) \tag{28}$$

After spectral factorization, there is no need to calculate the norm of $H_{clk}(\omega)$. In this way, the tedious calculation can be spared.

It is intended to analyze LCI tracking loops in z-domain. There are two reasons for doing so. On the one hand, most GNSS carrier phase tracking loops are developed in digital form. On the other hand, NCO is modeled as $\frac{1}{s}$ in s-domain, which cannot reflect the update rate difference between local and multichannel cooperative loop.

In z-domain, the transfer function is expressed as:

$$H_{clk}(z) = \frac{1}{1 + G(z)V_g(z) + F(z)V_f(z)} \tag{29}$$

where $V_g(z)$ and $V_f(z)$ represent the NCO update of local and multichannel cooperative loop respectively:

$$\begin{aligned} V_g(z) &= \frac{T_g z^{-1}}{1 - z^{-1}} \\ V_f(z) &= \frac{T_f z^{-1}}{1 - z^{-1}} \end{aligned} \tag{30}$$

where T_g and T_f denote the NCO update period of local and multichannel cooperative loop.

There are multiple combinations of $F(z)$ and $G(z)$. Taking second-order $F(z)$ and first-order multichannel cooperative loop filter as an example, the loop filters are presented by:

$$\begin{aligned} F(z) &= a_2\omega_n + \frac{T_f}{2}\frac{1 + z^{-1}}{1 - z^{-1}}\omega_n^2 \\ G(z) &= g_n \end{aligned} \tag{31}$$

where g_n, ω_n and a_2 are constant values related to the bandwidth of the tracking loop. Rearranging (31) results in:

$$F(z) = \frac{a_0 z + a_1}{z - 1} \tag{32}$$

where

$$\begin{aligned} a_0 &= a_2\omega_n + \frac{T_f}{2}\omega_n^2 \\ a_1 &= -a_2\omega_n + \frac{T_f}{2}\omega_n^2 \end{aligned} \tag{33}$$

The transfer function of oscillator phase noise can be derived as:

$$H_{clk}(z) = \frac{z^2 - 2z + 1}{z^2 + c_0 z + c_1} \tag{34}$$

where

$$\begin{aligned} c_0 &= g_n T_g + a_0 T_f - 2 \\ c_1 &= -g_n T_g + a_1 T_f + 1 \end{aligned} \tag{35}$$

The transfer function with other filter designs can be derived in the same way mentioned here.

The equivalence of integration approximation $\frac{1}{s}$ and analog discrete-time integrator $\frac{z^{-1}}{1-z^{-1}}$ is utilized to derive the equivalent discrete-time spectral density of $S_c^+(s)$, which can be expressed as:

$$S_c^+(z) = (2\pi f_0)\left(\frac{\sqrt{0.5h_0}}{z - 1} + \frac{\sqrt{2\pi^2 h_{-2}}}{(z-1)^2}\right) \tag{36}$$

Then the discrete-time form of (27) is derived as:

$$\sigma_{clk}^2 = \frac{1}{2\pi T_g}\int_{-\pi}^{\pi} H_{clk}(e^{j\omega}) S_c^+(e^{j\omega}) d\omega \tag{37}$$

where $H_{clk}(e^{j\omega})$ and $S_c^+(e^{j\omega})$ can be provided by (34) and (36).

Tracking error induced by thermal noise

Simplifying algebraically the second row of (22) results in:

$$\boldsymbol{\gamma_r} = (\beta_1^{-1}\beta_3 + \frac{\beta_1^{-1}\beta_2}{\beta_1 + \beta_2}\mathbf{e}\mathbf{d}^T)\boldsymbol{\phi} \tag{38}$$

For a specific channel, the equation becomes:

$$\gamma_r^{(i)} = \beta_1^{-1}\beta_3\phi^{(i)} + \left(\frac{\beta_1^{-1}\beta_2}{\beta_1 + \beta_2}\right)\frac{1}{N}\sum_{k=1}^{N}\phi^{(k)} \tag{39}$$

It is shown that the transfer function not only depends on the input phase of the channel itself but is dependent on the input phases of all channels used to estimate the oscillator phase error. Therefore, the transfer function of a specific channel cannot be derived directly (Shafaati et al. 2015).

The solution is to transform the second part of (39) into an equivalent normal tracking loop stimulated by a signal with the variance which is the same as $\frac{1}{N}\sum_{k=1}^{N}\phi_k$. When local filter is excluded, in other words, $F(s)=0$, the first part of (39) equals to 0 and the equation becomes:

$$\gamma_r^{(i)} = \left(\frac{G(s)}{s+G(s)}\right)\frac{1}{N}\sum_{k=1}^{N}\phi^{(k)} \tag{40}$$

The equation above can be considered as a simple tracking loop stimulated by $\frac{1}{N}\sum_{k=1}^{N}\phi^{(k)}$, whose variance is $\chi^2 = \frac{1}{N^2}\sum_{k=1}^{N}\phi^2$. Since $\phi^{(i)} \sim N(0,\sigma_i^2)$, the multi-input tracking loop can be assumed to be a single input one with only $\phi^{(i)}$ as its input, but with a gain factor $\frac{\chi}{\sigma_i}$. Therefore, the $\frac{1}{N}\sum_{k=1}^{N}\phi^{(k)}$ will be replaced by:

$$\frac{1}{N}\sum_{k=1}^{N}\phi^{(k)} = \frac{\chi}{\sigma_i}\phi^{(i)} = \alpha_i\phi^{(i)} \tag{41}$$

So the transfer function due to thermal noise of the ith channel is expressed as:

$$H_r(s) = \frac{F(s)(s+F(s)) + G(s)(F(s)+\alpha_i s)}{(F(s)+s)(s+F(s)+G(s))} \tag{42}$$

With the equivalence of integration from s-domain $\frac{F(s)}{s}$ to z-domain $F(z)V(z)$, the corresponding z-domain model of (42) is derived as:

$$H_r(z) = \frac{H_f(z)(1+H_f(z)) + H_g(z)(H_f(z)+\alpha_i)}{(1+H_f(z))(1+H_f(z)+H_g(z))} \tag{43}$$

where

$$\begin{aligned} H_f(z) &= F(z)V_f(z) \\ H_g(z) &= G(z)V_g(z) \end{aligned} \tag{44}$$

Also, Eq. (43) can be expressed as a rational function:

$$H_r(z) = \frac{c_0z^4 + c_1z^3 + c_2z^2 + c_3z + c_4}{d_0z^4 + d_1z^3 + d_2z^2 + d_3z + d_4} \tag{45}$$

where the c and d parameters are dependent on the design of loop filters $F(z)$ and $G(z)$. As the mathematical expressions of these parameters are very cumbersome, they will not be shown here.

Since the thermal noise transfer function is derived, the tracking error of LCI loops can be derived through the equivalent bandwidth. The equivalent bandwidth is evaluated using:

$$B_n = \frac{1}{2\pi T_f}\int_{-\pi}^{\pi}|H_r(e^{i\omega})|^2 d\omega \tag{46}$$

where $H_r(e^{i\omega})$ is provided by (45).

Then the white Gaussian thermal noise-induced tracking error of LCI tracking loops is derived as:

$$\sigma_c^2 = \frac{B_n}{C/N_0}\left(1+\frac{1}{2T_fC/N_0}\right) \tag{47}$$

Although the equation of LCI tracking error induced by thermal noise resembles that of a typical PLL, the equivalent loop bandwidth B_n of LCI is dependent on the design of both multichannel cooperative and local loop, which is quite different from the PLL equivalent bandwidth. B_n of LCI will be calculated through numerical integration in a computer.

LCI tracking loops performance tests and analysis

The performance of LCI architecture will be tested and analyzed through simulation and real GNSS signals in this section. The correctness of the LCI measurement error model from the previous section will be validated, and the performance of LCI architecture will be explored.

Semi-analytic simulation

A semi-analytic simulation is conducted to validate the LCI theoretical model. The simulation is developed based on the open-source semi-analytic tracking loop simulations (SATL-Sim) toolbox by PLAN Group, Calgary (Borio et al. 2011). The simulation diagram is shown in Fig. 6.

The simulation achieves a compromise between accuracy and efficiency with the principle that the integrate and dump block, which is the most computationally demanding component, is replaced with its accurate analytical model. In Fig. 6, analytical models of integration signal apply to the two signal generation blocks, one for the multichannel cooperative loop and one for the long coherent local tracking loop. The oscillator discriminator block also accepts integration signals from all other channels used to estimate the effects of the receiver oscillator. The short time integration signal will be generated using the following expression directly:

$$\mathbf{r_g}(k) = sinc\left(f_g(k)\cdot T_g\right)e^{i\theta_{e,g}(k)} \tag{48}$$

Assuming the integration starts at time t_0, and the initial phase error is θ_0, then $\theta_{e,g}(k)$ can be expressed as:

$$\theta_{e,g}(k) = f_g(k)(t_0 + \frac{T_g}{2}) + \theta_0 \tag{49}$$

where $\theta_{e,g}(k)$ is the average phase through the integration period. The long coherent integration signal generation can be expressed as:

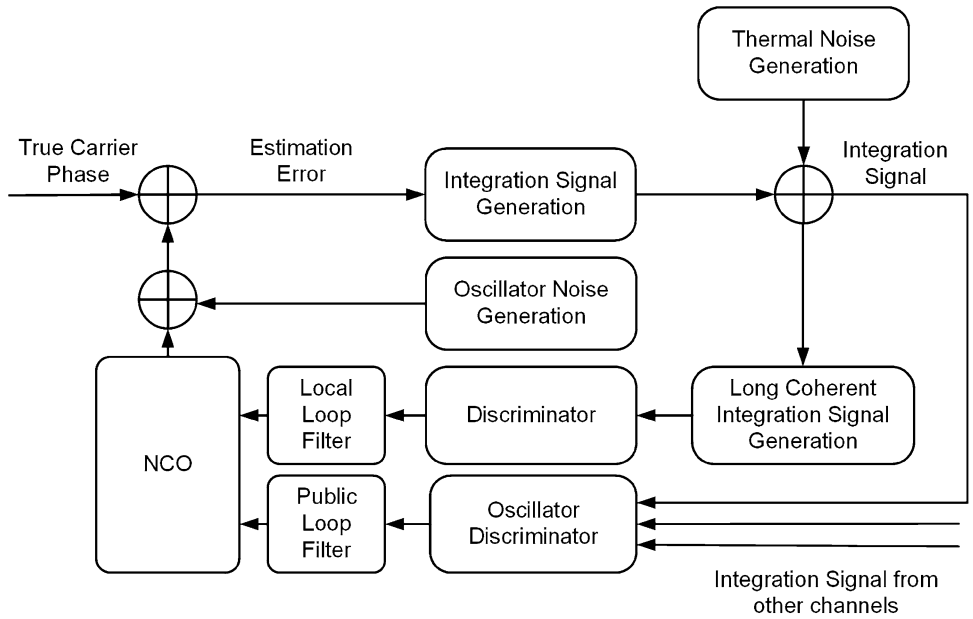

Fig. 6 Semi-analytic simulation diagram of LCI tracking architecture. Thermal noise is added after the generation of integration signals, and the oscillator noise is added after the NCO update

$$\mathbf{r_f}(n) = \mathrm{sinc}\left(f_e T_{coh}\right) e^{j\theta_e} \tag{50}$$

Since during the long integration period, the frequency and phase of the local signal replica have been adjusted several times, the term $f_e T_{coh}$ can be denoted as:

$$f_e T_{coh} = \sum_{k=1}^{N_r} \left(f_g(k) \cdot T_g\right) \tag{51}$$

where $N_r = T_{coh}/T_g$ is the integration time ratio between local and multichannel cooperative loop. So the expression of f_e can be derived:

$$f_e = \frac{1}{N_r} \sum_{k=1}^{N_r} f_g(k) \tag{52}$$

The phase error of the long coherent integration signal (θ_e) is denoted as:

$$\theta_e = f_e \left(t_0 + \frac{T_{coh}}{2} \right) + \theta_0 \tag{53}$$

Thermal noise is modeled as additive white Gaussian noise, and the two-state clock model is adopted. Different types of oscillators are simulated, whose h-parameters are shown in Table 1 (Curran et al. 2012).

The simulation results in Fig. 7 are conducted using second-order local PLL with 200 ms integration time, 2 Hz bandwidth and second-order multichannel cooperative loop with 10 ms integration time, 5 Hz bandwidth. Solid and dashed lines represent the theoretical and simulated tracking jitters, respectively. The theory and simulation curves are obviously highly consistent, proving that the theoretical analysis is correct. As the signal C/N_0 decreases, the thermal noise becomes the dominant error resource, leading to the trend of convergence of all three curves. In those regions for high C/N_0 values, the dominant error resource is the Allan deviation oscillator phase noise, and the tracking error is dependent on the quality of oscillators. Admittedly, with a poorer oscillator comes greater tracking jitters. When an OCXO oscillator is adopted, the tracking jitters are slightly bigger than when there is only thermal noise. The adoption of a TCXO represents the largest tracking jitters, which is reasonable for the existence of higher oscillator phase noise.

Table 1 Simulation oscillator h-parameter. The parameters of a typical TCXO and OCXO are provided

Oscillator	h_0	h_{-2}
TCXO	$1.9 * 10^{-21}$	$2.5 * 10^{-23}$
OCXO	$2.6 * 10^{-22}$	$4.0 * 10^{-26}$

It is the multichannel cooperative loop that dominates the tracking of oscillator phase errors. Figure 8 shows the tracking jitters of LCI loops with different bandwidths of the multichannel cooperative loop when the TCXO is adopted, and the local loop is configured as 200 ms, 1 Hz. For small C/N_0 values, different bandwidths do not make much of a difference because the dominant error is the thermal noise. For high C/N_0 values where oscillator instability dominates, however, as multichannel cooperative loop bandwidth increases, tracking jitters become smaller. The results indicate that the negative influence of oscillator instability can principally be reduced by increasing the multichannel cooperative loop bandwidth.

As the multichannel cooperative loop takes care of most of the high-frequency oscillator phase errors, the integration

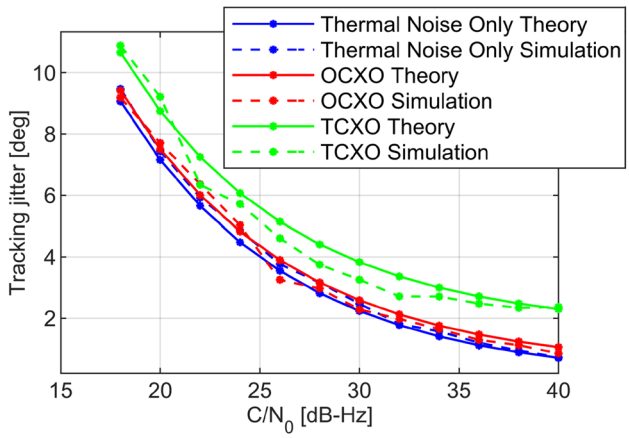

Fig. 7 Oscillator and thermal noise effects on tracking jitter of LCI tracking loops with 200 ms, 1 Hz local loop and 10 ms 5 Hz multichannel cooperative loop. Two different types (typical OCXO and TCXO) of oscillators are simulated, and the simulation with thermal noise alone is also conducted

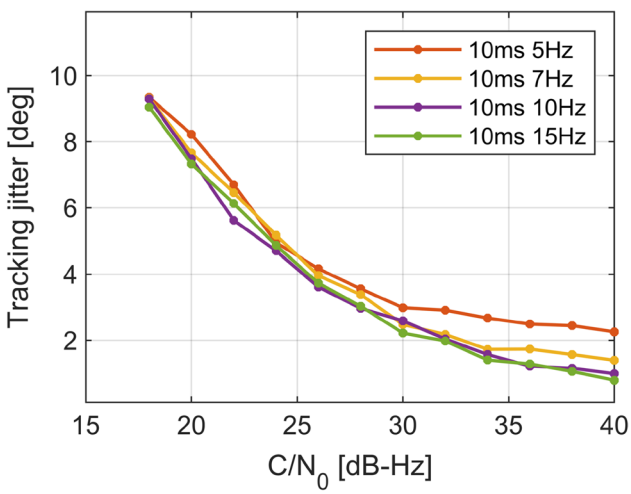

Fig. 8 Tracking jitters of LCI loops with different multichannel cooperative loop bandwidths when equipped with 200 ms, 1 Hz local loop. Increasing bandwidth of multichannel cooperative loop helps to reduce the tracking jitters of LCI loops

time of the local loop can be increased further to track weaker signals. The LCI sensitivity simulation test results are shown in Fig. 9. During the test, the signals are polluted with the TCXO noise mentioned above. The multichannel cooperative loop is configured as 10 ms, 15 Hz. In contrast to a typical PLL tracking loop with a sensitivity of 28 dB-Hz, LCI tracking architecture enables the local tracking loop to perform an integration time of several seconds. The testing results indicate that when the local loop performs up to 3 s of integration time, LCI tracking architecture is capable of tracking 6 dB-Hz signals with carrier phase jitters around 5 degrees.

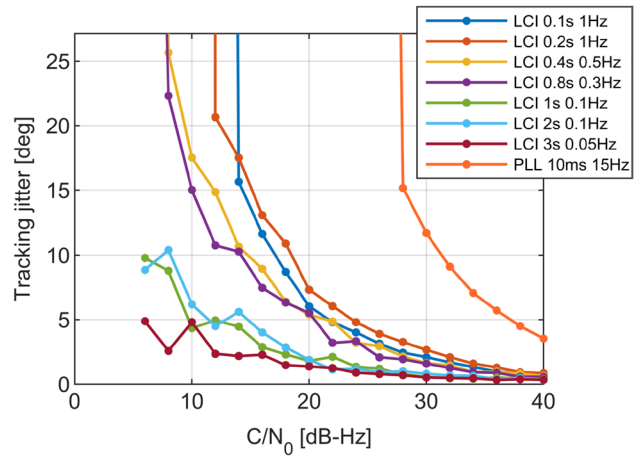

Fig. 9 Tracking jitters of LCI loops with different local loop coherent periods when equipped with 10 ms, 15 Hz multichannel cooperative loop. With a longer integration period and narrower local loop bandwidth, the tracking jitters of LCI loops are smaller

Real world signal tests

The performance of LCI loops is evaluated through real-world signal tests in this section. The experiment setup will be introduced in the first place. Then the test results are analyzed on two different levels: the signal power and the observation accuracy.

Experiment setup

About 10 min of GNSS RF signals from a stationary rooftop-mounted antenna was recorded by Spirent GSS6425: a multiple constellation record playback system (RPS). Spirent GSS6425 records the RF data with an oven controlled crystal oscillator (OCXO) as its reference, which gives a reference frequency reading within ± 0.02 Hz of the nominal frequency. The RF signals will be down-converted to IF and stored on the internal hard disk. A software defined GNSS receiver developed by I2Nav Group (I2xSNR) with LCI tracking loops is used to process the IF signals. In the process of data recording, the RF signals were also sent to a reference GNSS receiver through a splitter. The carrier phase observations from the reference receiver will be used to conduct a zero-baseline analysis later on.

As can be seen in Fig. 10, there were 6 GPS satellites in line of sight (LOS). All satellite signals are above 35 dB-Hz. Two types of tests will be conducted. The first test evaluates the signal power after long integration. The second test explores the sensitivity of LCI tracking loops.

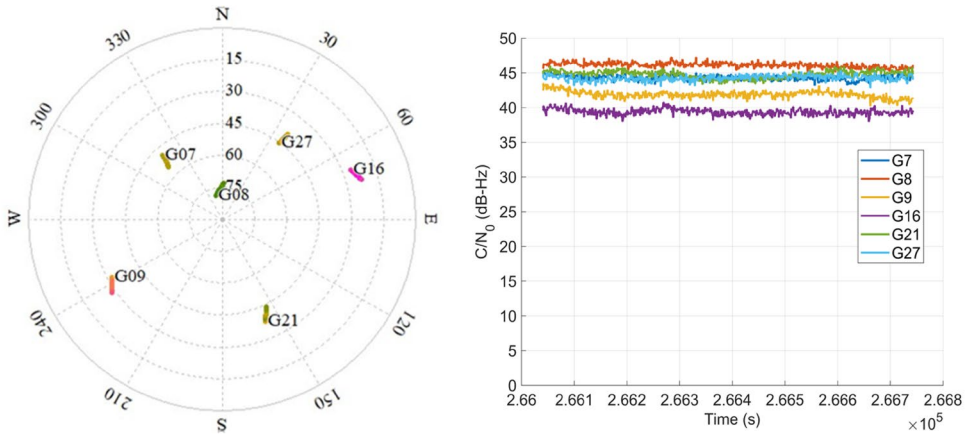

Fig. 10 Visible satellites and their C/N_0 values in real-world signal test. The left panel is the space distribution of visible satellites during the experiment. The right panel shows visible satellites' C/N_0 values

Signal power test of long coherent integration

As mentioned in the Methodology section, when coherent integration time increases, oscillator phase noise will cause signal power degradation along the sinc-squared characteristic. This test will explore how well the LCI system can suppress oscillator noise during long integration.

A comparison landmark is needed in the first place, which is the theoretical maximum power that the signal can integrate during the integration process. This power can be evaluated by measuring the peak power of a short integration period, for example, 100 ms, and then scaling it with a gain factor expected due to longer integrations. The gain factor can be obtained by dividing the long integration time by the landmark integration time. In other words, assuming the landmark short integration time is 100 ms, then the theoretical peak power of a long coherent integration, for example, 1 s, should be 1 s/100 ms = 10 times as large as that of the landmark integration time. This is reasonable for the clock errors are insignificant enough to be ignored when short time integration time is adopted.

The GNSS signals are processed by digital channels, after the integration-and-dump operation, the output values will be used to evaluate the signal power directly. Hence, the signal power has no physical unit. Figure 11 displays the signal power of satellites 7 and 9 with an integration period 100 ms. Satellite 7 has a higher elevation angle and carrier-to-noise ratio (C/N_0), so its signal power is higher.

The performance of LCI and PLL tracking loops will be tested and compared. The landmark integration time is set as 100 ms. The reason for choosing 100 ms is that the thermal noise can be suppressed properly under this configuration. In addition, since GSS6425 PRS adopted an OCXO as its clock reference, the clock noise effect of 100 ms integration time is insignificant. The peak power of longer integration time will be divided by the gain factor to be normalized to the landmark level. Peak power results are shown in Fig. 12, and the means of the measured peak power are given in Table 2.

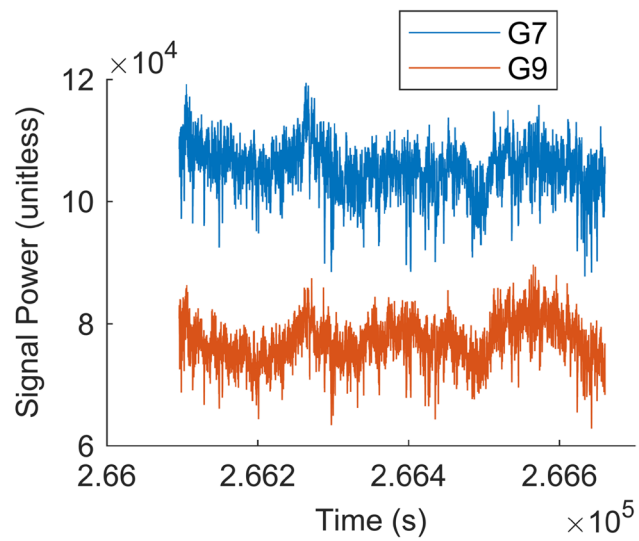

Fig. 11 Unitless signal power of satellite 7 and 9. With higher elevation angle and C/N_0 values, the signal power of satellite 7 is higher than that of satellite 9

In the context of traditional PLL tracking loops, although the mean power of 200 ms integration time shows no difference from that of the landmark in Table 2, the high frequency noise caused by the oscillator appears on the green line in Fig. 12. Clock instability causes around 30 (PRN 7) and 10 (PRN 9) dB of power attenuation as the PLL integration time increases up to 400 ms. When the integration period increases to 600 ms, there is no valid power accumulated in the PLL tracking loop, which indicates the loop has lost tracking. On the contrary, LCI tracking architecture can perform coherent integration for up to 3 s without power loss. The multichannel cooperative loop in LCI tracking architecture is dedicated to estimating the common oscillator phase error with a high frequency, which guarantees the conduction of super-long coherent integration time.

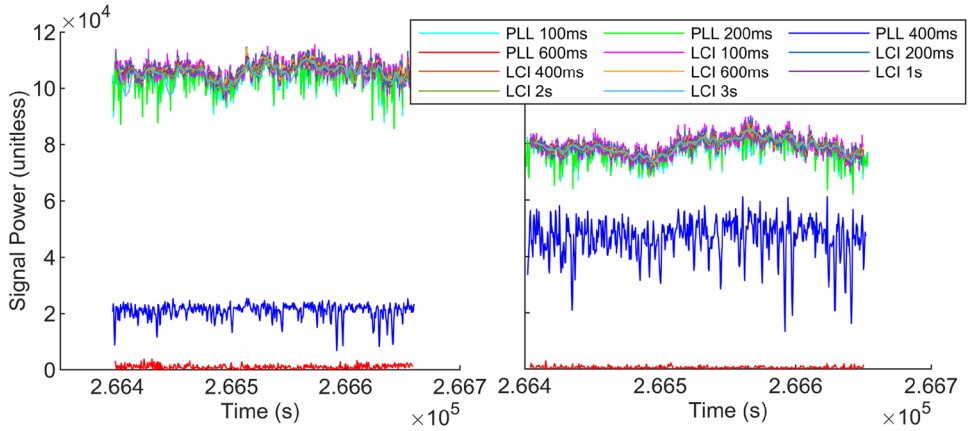

Fig. 12 Signal power of satellite 7 (left panel) and 9 (right panel) with different loops and integration periods. As integration time increases, the normalized peak power of PLL loops decreases rapidly for the existence of oscillator induced errors while LCI loops show no power degradation

Table 2 Signal power measurements of different loops and integration periods (unitless). Results of satellites 7 and 9 are shown

Integration time	PRN 7	PRN 9
PLL 100 ms	104,476.5	77,741.2
PLL 200 ms	104,384.1	77,674.3
PLL 400 ms	20,911.7	46,535.2
PLL 600 ms	1054.6	567.7
LCI 100 ms	106,542.8	79,298.2
LCI 200 ms	106,538.7	79,290.2
LCI 400 ms	106,533.1	79,281.9
LCI 600 ms	106,539.5	79,268.0
LCI 1 s	106,428.4	79,241.1
LCI 2 s	106,006.6	79,194.7
LCI 3 s	105,242.9	79,112.8

Carrier phase tracking sensitivity test

The GNSS carrier phase tracking sensitivity of LCI tracking architecture is explored in this test. With the software defined GNSS receiver as the testing platform, the weak signals are generated by adding a certain amount of white Gaussian noise to the IF signals. The strength of the addictive noise can be set by the noise generating software so that quantitative tests are feasible.

Satellites 7 and 9 are selected as testing channels whose signal strength will be degraded gradually, and the quality of their carrier phase observations will be evaluated. In order to detect the cycle slip, the zero-baseline triple-difference carrier phase measurements between the reference receiver and the LCI SDR will be evaluated, leaving only the cycle slip quantity in the result. If over a half-cycle slip happens, the channel will be determined as loss of tracking.

Cycle slip results are shown in Fig. 13. The upper half figure shows the C/N_0 of the input signal. Below is the cycle slip evaluation result. The weakest signal a PLL loop can track is around 28 dB-Hz, while LCI loops can track weak signals below 10 dB-Hz. In the context of LCI with 200 ms local loop, the channel of satellite 9 lost lock when GNSS signal was about 7 dB-Hz. Since 200 ms of integration is not long enough to suppress the increasing thermal noise, the carrier phase noises of both satellites are large. LCI tracking architecture with 3 s integration period and 0.008 Hz bandwidth can not only track the extremely weak GNSS carrier phase signals, in this case, 6 dB-Hz, but it can track them with extremely high accuracy. The zero-baseline triple-difference carrier phase standard deviation (std) of satellites 7 and 9 is 4.0 and 3.6 degrees, which agrees with the simulation results above. Orange lines in Fig. 13 show that when tracking extremely weak signals, there is no accuracy degradation compared to tracking strong signals.

Conclusion

This paper has addressed the problem of tracking GNSS carrier phase using long coherent integration period. Specifically, the oscillator instability-induced effects have been considered. A multichannel cooperative tracking architecture: LCI tracking architecture is proposed to perform extreme long coherent integration time by using a dedicated multichannel cooperative to track the effects of oscillator. The digital transfer function of LCI is derived. Then the LCI tracking errors induced by oscillator instability and thermal noise are evaluated. To validate and test this tracking architecture, semi-analytic simulation and real GPS L1 signal experiments are conducted. It has been shown that LCI tracking loops can track 6 dB-Hz GNSS signals with carrier phase accuracy of around 4 degrees, providing superior tracking to traditional PLL loops when subject to thermal and oscillator noise. In future, additional study would be required to determine the performance of LCI arthitecture under dynamic conditions. Different grades of IMUs will be adopted to compensate the dynmamics and their impacts are

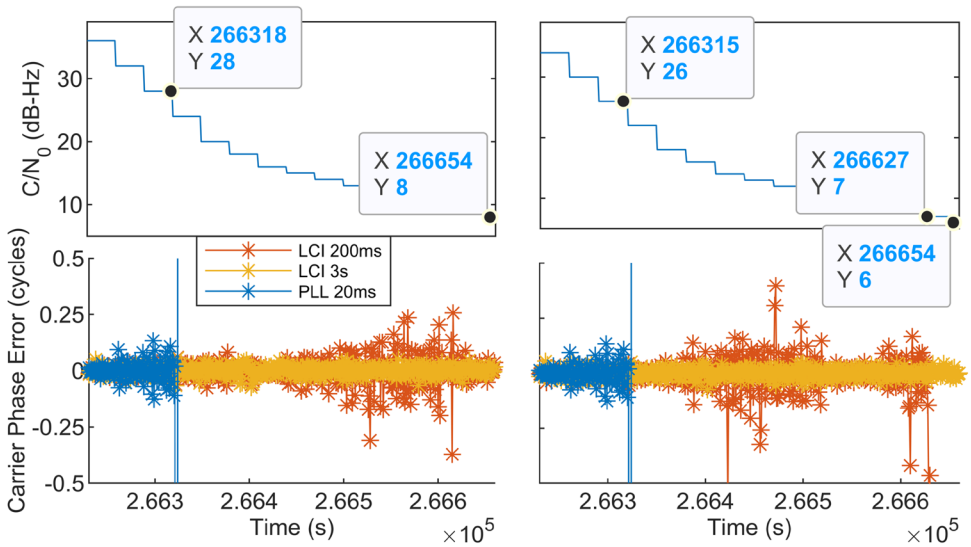

Fig. 13 Weak signal test of satellites 7 (left) and 9 (right) with different loops and integration periods. PLL loops lose lock just after C/N_0 drops below 30 dB-Hz, yet LCI loops with long coherent integration time can track 6 dB-Hz carrier phase accurately

to be evaluated. Future research also requires exploring the multipath suppressing ability of LCI architecture.

Acknowledgements This research is funded by the National Key Research and Development Program of China (No. 2020YFB0505803) and the National Natural Science Foundation of China (No. 41974024)

Data Availability The data used in this manuscript are available from the corresponding author upon request.

References

Alban S, Akos DM, Rock SM (2003) Performance analysis and architectures for INS-aided GPS tracking loops. In: Proc. ION NTM 2003, Institute of Navigation, Anaheim, CA, January 22–24, pp 611–622

Bernal D, Closas P, Fernandez-Rubio JA (2008) Particle filtering algorithm for ultra-tight GNSS/INS integration. In: Proc. ION GNSS 2008, Institute of Navigation, Savannah, GA, September 16–19, pp 2137–2144

Bresson G, Alsayed Z, Yu L, Glaser S (2017) Simultaneous localization and mapping: a survey of current trends in autonomous driving. IEEE Trans Intell Veh 2(3):194–220

Borio D, Anantharamu PB, Lachapelle G (2011) SATLSim: a semi-analytic framework for fast GNSS tracking loop simulations. GPS Solut 15(4):427–431

Chen S, Gao Y, Lin T (2017) Effect and mitigation of oscillator vibration-induced phase noise on carrier phase tracking. GPS Solut 21(4):1515–1524

Curran JT, Lachapelle G, Murphy CC (2012) Digital GNSS PLL design conditioned on thermal and oscillator phase noise. IEEE Trans Aerosp Electron Syst 48(1):180–196

Gaggero PO (2008) Effect of oscillator instability on GNSS signal integration time. Dissertation, University of Neuchtel

Gowdayyanadoddi NS, Broumandan A, Curran JT, Lachapelle G (2014) Benefits of an ultra stable oscillator for long coherent integration. In: Proc. ION GNSS+ 2014, Institute of Navigation, Tampa, Florida, September 8–12, pp 1578–1594

Groves PD, Zhong Q, Faragher R, Esteves P (2020) Combining inertially-aided extended coherent integration (supercorrelation) with 3D-mapping-aided GNSS. In: Proc. ION GNSS+ 2020, Institute of Navigation, September 21–25, pp 2327–2346

Irsigler M, Eissfeller B (2002) PLL tracking performance in the presence of oscillator phase noise. GPS Solut 5(4):45–57

Kaplan ED, Hegarty C (2017) Understanding GPS/GNSS: principles and applications. Artech house

Kuutti S, Fallah S, Katsaros K, Dianati M, Mccullough F, Mouzakitis A (2018) A survey of the state-of-the-art localization techniques and their potentials for autonomous vehicle applications. IEEE Internet Things J 5(2):829–846

Niu X, Ban Y, Zhang Q, Zhang T, Zhang H, Liu J (2015) Quantitative analysis to the impacts of IMU quality in GPS/INS deep integration. Micromachines 6(8):1082–1099

O'Driscoll C, Petovello MG, Lachapelle G (2011) Choosing the coherent integration time for Kalman filter-based carrier-phase tracking of GNSS signals. GPS Solut 15(4):345–356

Pany T, Euler H, Winkel J (2011) Indoor carrier phase tracking and positioning with difference correlators. In: Proc. ION GNSS 2011, Institute of Navigation, Portland, OR, September 20–23, pp 2202–2213

Pany T, Kaniuth R, Eissfeller B (2005) Deep integration of navigation solution and signal processing. In: Proc. ION GNSS 2005, Institute of Navigation, Long Beach, CA, September 13–16, pp 1095–1102

Pany T, Riedl B, Winkel J, Wörz T, Schweikert R, Niedermeier H et al (2009) Coherent integration time: the longer, the better. Inside GNSS 4(6):52–61

Pany T et al (2009) Performance of a partially coherent ultra-tightly coupled GNSS/INS pedestrian navigation system enabling coherent integration times of several seconds to track GNSS signals down to 1.5 dBHz. In: Proc. ION GNSS 2009, Institute of Navigation, Savannah, GA, September 22–25, pp 919–934

Rebeyrol E, Julien O, Macabiau C, Ries L, Delatour A, Lestarquit L (2007) Galileo civil signal modulations. GPS Solut 11(3):159–171

Ren T, Petovello MG (2017) A stand-alone approach for high-sensitivity GNSS receivers in signal-challenged environment. IEEE Trans Aerosp Electron Syst 53(5):2438–2448

Shafaati A, Lin T, Lachapelle G (2015) Performance comparison of difference correlator and co-op tracking architectures under receiver clock instability. In: Proc. ION GNSS+ 2015, Institute of Navigation, Tampa, Florida, September 14–18, pp 2887–2904

Soloviev A, Dickman J (2011) Extending GPS carrier phase availability indoors with a deeply integrated receiver architecture. IEEE Wirel Commun 18(2):36–44

Thombre S, Raasakka J, Hurskainen H, Nurmi J, Valkama M, Lohan S (2011) Local oscillator phase noise effects on phase angle component of GNSS code correlation. In: Proc. ICL-GNSS 011, IEEE, Tampere, Finland, June 29–30, pp 110–115

Van Diggelen FST (2009). A-GPS: Assisted GPS, GNSS, and SBAS. Artech house

Watson R, Lachapelle G, Klukas R (2006) Testing oscillator stability as a limiting factor in extreme high-sensitivity GPS applications. In: Proc. ENC 2006, Manchester, UK, 8–10 May 2006

Zhang T, Ban Y, Niu X, Guo W, Liu J (2017) Improving the design of MEMS INS-aided PLLs for GNSS carrier phase measurement under high dynamics. Micromachines 8(5):135

Zhang X, Tao X, Zhu F, Shi X, Wang F (2018) Quality assessment of GNSS observations from an Android N smartphone and positioning performance analysis using time-differenced filtering approach. GPS Solut 22(3):1–11

Zhang Z, Li B, Nie L, Wei C, Jia S, Jiang S (2019) Initial assessment of BeiDou-3 global navigation satellite system: signal quality, RTK and PPP. Gps Solut 23(4):1–12

Zhodzishsky MI, Kurynin RV, Veitsel AV (2020) A radical approach to reducing effects of quartz crystal oscillator instability on GNSS receiver performance. In: Proc. SYNCHROINFO, IEEE, Svetlogorsk, Russia, July 01–03, pp 1–18

Zhodzishsky M, Yudanov S, Veitsel V, Ashjaee J (1998) Co-op tracking for carrier phase. In: Proc. ION GPS 1998, Institute of Navigation, Nashville, TN, September 15–18, pp 653–664

Zhuo L (2019) Research on deep integration technology for GNSS carrier phase quality in complex signal environment. Dissertation, Wuhan University

Publisher's Note Springer Nature remains neutral with regard to jurisdictional claims in published maps and institutional affiliations.

Springer Nature or its licensor (e.g. a society or other partner) holds exclusive rights to this article under a publishing agreement with the author(s) or other rightsholder(s); author self-archiving of the accepted manuscript version of this article is solely governed by the terms of such publishing agreement and applicable law.

Xin Feng received the B.E and M.E degrees from Wuhan University, Wuhan, China, in 2018 and 2021, respectively. He is pursuing a Ph.D. degree in geodesy and survey engineering with the School of Geodesy and Geomatics, Wuhan University. His primary research interests include GNSS receiver and Multi-sensor ultra-tightly integrations.

Tisheng Zhang is an associate professor in GNSS Research Center at Wuhan University, China. He holds a B.SC. and a Ph.D. in Communication and Information System from Wuhan University, Wuhan, China, in 2008 and 2013, respectively. From 2018 to 2019, he was a postdoctoral researcher at the Hong Kong Polytechnic University. His research interests focus on the fields of GNSS receiver, multi-sensor deep integration and robot navigation.

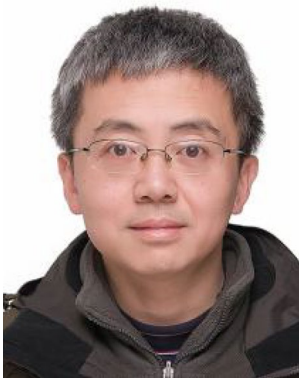

Xiaoji Niu is currently a Professor with the GNSS Research Center, Wuhan University, China. He has published more than 90 academic papers and owns 28 patents. He leads a multi-sensor navigation group focusing on GNSS/INS integration, low-cost navigation sensor fusion and its new applications.

Thomas Pany is a full professor at Universität der Bundeswehr München at the faculty of Aerospace Engineering, where he teaches satellite navigation. He focuses on GNSS/LTE/5G signal design and processing, software receivers and GNSS/INS/LiDAR fusion and has about 200 publications, including patents and one monography.

Jingnan Liu member of the Chinese Academy of Engineering, professor, and Ph. D supervisor. He is an expert in geodesy and surveying engineering with a specialty in GNSS technology and applications. He has been engaged in the research of geodetic theories and applications, including national coordinate systems, GNSS technology and software development, as well as large project implementations.